

Intensities of Mössbauer diffractions from polycrystalline bcc ^{57}Fe

U. Kriplani,¹ J. Y. Y. Lin,¹ M. W. Regehr,^{1,2} and B. Fultz¹

¹California Institute of Technology, W. M. Keck Laboratory, mail 138-78, Pasadena, California 91125

²Jet Propulsion Laboratory, Mail 171-113, Pasadena, California 91125

(Received 4 May 2001; published 10 December 2001)

Diffraction patterns were measured on a polycrystalline bcc ^{57}Fe foil using a Mössbauer powder diffractometer with high sensitivity. Measurements with and without a magnetic field normal to the scattering plane showed large differences in the diffracted intensities of the different nuclear resonances. These magnetic effects on diffraction intensities were interpreted successfully with a single scattering theory developed to handle isotropic and anisotropic orientation distributions of hyperfine magnetic fields. When there is coherent interference between nuclear scattering and x-ray Rayleigh scattering, an asymmetry in the coherent intensity of the three pairs of diffractions for the ^{57}Fe magnetic sextet (1,6), (2,5), (3,4) is predicted. This is largest in the presence of a uniaxial magnetic field, and the calculated and measured asymmetries were in good agreement. A reduced diffraction intensity for lines (2,5) and (3,4) caused by spin-flip incoherence was also measured. The effects of dynamical diffraction, if present, are shown to be small.

DOI: 10.1103/PhysRevB.65.024405

PACS number(s): 76.80.+y, 61.18.Fs, 61.10.-i

I. INTRODUCTION

Mössbauer diffraction occurs when the coherent scattering of nuclear resonant photons leads to the formation of diffraction peaks. It is analogous to how Rayleigh scattering of x rays provides x-ray diffraction peaks. The coherence of Mössbauer scattering was first studied by Black and Moon,¹ and the first Mössbauer diffraction measurements were performed a few years later.² Diffraction physics with x rays, electrons, and neutrons is sometimes classified into phenomena based on kinematical (single-scattering) or dynamical (multiple-scattering) theories. The dynamical theory of Mössbauer diffraction³⁻⁶ is expected to be generally valid, but the most interesting phenomena of dynamical theory occur in large single crystals when there is a significant probability that a photon will undergo multiple coherent scatterings. Experimental work on dynamical Mössbauer diffraction includes measurements of the speed-up of the decay of the nuclear excitation through strong coherent channels.^{7,8} This enhancement of coherent channels causes them to dominate over incoherent internal conversion channels, making diffraction peaks easier to measure.

Because hyperfine interactions give Mössbauer diffraction a sensitivity to both chemical species and magnetic fields, Mössbauer diffraction is a unique tool for studying atomic-scale structures of condensed matter. For studies of atom arrangements in solids, however, dynamical diffraction³⁻⁶ is not as useful as kinematical theory.^{9,10} Kinematical Mössbauer diffraction, which is expected with small or structurally defective crystals, unfortunately suffers from comparatively low count rates. Tegze and Faigel¹¹ built a focusing Mössbauer diffractometer and measured energy spectra during the diffraction of a polycrystalline iron sample. Full diffraction patterns were first measured on polycrystals by Stephens *et al.*¹² Mössbauer diffraction has successfully employed hyperfine interactions to select the chemical environment of the diffracting species.¹³ The signal-to-noise ratios of previous measurements have been inadequate for quantitative measurements of powder diffraction intensities. In this

paper we present experimental data from a Mössbauer diffractometer having a signal-to-noise ratio sufficient for quantitative measurements of diffraction peak intensities from polycrystalline ^{57}Fe .

Powder diffraction patterns provide quantitative information on structure, phase fractions, and defect densities in materials and condensed matter. For Mössbauer diffraction patterns to be used quantitatively, it must be understood how the intensities of Mössbauer diffraction peaks depend on diffraction angle and state of magnetization in the sample. The “Lorentz-polarization factor,” for example, is an analogous feature affecting the intensities of x-ray powder diffraction peaks.¹⁴ It depends on the orientation of the electric dipole moment induced in the atomic electrons along the direction of the photon electric field. Such classical dipole radiation pictures are inadequate for Mössbauer diffraction patterns, however. Nuclear radiation fields (magnetic dipole for ^{57}Fe) are quantized with respect to the direction of the hyperfine magnetic field at the nucleus, and are only partially aligned along the field directions of the incident photon. The intensities of Mössbauer diffraction peaks also depend on the probabilities and resonance energies of the nuclear transitions.

An analytical form for the polarization factor with anisotropic distributions of hyperfine magnetic fields is developed and is used in a kinematical theory of the intensities of Mössbauer diffractions. The calculated and measured intensities are compared for different nuclear transitions and external magnetic fields. The measurements showed a difference in diffraction intensities from pairs of nuclear transitions with opposite angular momentum, such as peaks 1 and 6 in the magnetic sextet, ($+\frac{1}{2} \rightarrow +\frac{3}{2}$) and ($-\frac{1}{2} \rightarrow -\frac{3}{2}$). This difference was interpreted as an effect of coherent interference between nuclear and Rayleigh x-ray scattering and was most evident in a uniaxial magnetic field. A “spin-flip incoherence” that suppresses diffractions from peaks 2 and 5 and peaks 3 and 4 in the magnetic sextet was also confirmed experimentally. It was not obvious that the kinematical theory is of quantitative value for interpreting diffraction pat-

terns from even small crystals, since the cross section for Mössbauer scattering is so large. It is interesting that good quantitative success of kinematical theory was found in the present work. Although the dynamical effects on coherent energy spectra were not measurable accurately, they appear to be small.

II. EXPERIMENT

The Mössbauer diffractometer consists of a position-sensitive detector mounted on the outer stage of a General Electric XRD-5 θ - 2θ goniometer, a ^{57}Co (Rh) radioactive source mounted on a Ranger Scientific VT-900 Doppler drive, and a horseshoe magnet that can be installed around the sample.¹⁵ The sample is mounted over the center of rotation of the goniometer and rotates at half the rate of the outer stage. The goniometer is driven by a stepper motor under control of a computer that automates the measurement and data acquisition. The outer stage and, thus, the detector rotate through a 45° range in steps of $0.000\,03^\circ$. A pair of slits, fitted near its exit with a Pb-Cu-Al graded shield with a $10\text{ mm} \times 2\text{ mm}$ opening, collimated the beam from the radioactive source. An external magnetic field was applied to the sample in the vertical direction with a permanent magnet having Nd-Fe-B pole pieces and a field of 3.3 kG.

The sample was a cold rolled and annealed foil of 90%-enriched ^{57}Fe . Two pieces of the foil were glued onto thin plastic sheet of 1 mm thickness, making a sample about $8\text{ mm} \times 15\text{ mm}$ in area. The sample was held firmly in a demountable stage that allowed accurate repositioning of the sample after removal.

The Siemens X-1000 area detector includes a chamber pressurized to approximately 4 bars with Xe gas. Locations of γ -ray detection are provided with a multiwire grid electrode, about $10\text{ cm} \times 10\text{ cm}$ in size. The detector subtended an angle of approximately 1 sr about the sample. The efficiency for 14.41 keV photons, measured by comparison with a photomultiplier tube of known efficiency, is better than 80%. The detector is controlled by a frame-buffer computer, which decodes the signals from the detector to provide position information for each detected photon.

The Doppler drive was operated in “constant velocity

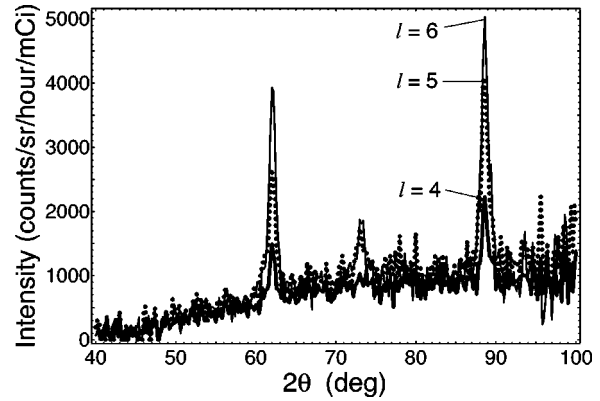


FIG. 2. Zero-field Mössbauer diffraction patterns of ^{57}Fe for transition lines $l=4$ (thick solid line), 5 (dotted line), and 6 (thin solid line).

mode,” where the ^{57}Co source moves at a constant velocity for part of the drive cycle. The detector was disabled electronically during that part of the cycle when the Doppler velocity was incorrect. To obtain diffraction patterns, the detector was rotated through a range of 2θ in steps of 1° . At each step, the frame-buffer computer acquired an image. The graphs of intensity versus 2θ of Figs. 1–3 were obtained from sets of 46 detector images by geometric transformation from the x - y coordinates of each pixel to the scattering angle 2θ . The intensity as a function of 2θ is calculated by sorting the detected photons into bins of 0.2° width and dividing the photon counts by the number of pixels contributing to each bin. The intensity distributions obtained from all the images are then superimposed with appropriate angle offsets to get wide-angle diffraction patterns that are averaged over the sensitivity variations across the detector.

III. RESULTS

Figure 1 presents measured intensities as functions of 2θ for the “ $l=6$ transition” from the sixth peak in the hyperfine sextet ($-\frac{1}{2} \rightarrow -\frac{3}{2}$). The off-resonance intensity (trace B) in Fig. 1 consists of a smoothly varying component and several sharp peaks. The smoothly varying intensity originates with

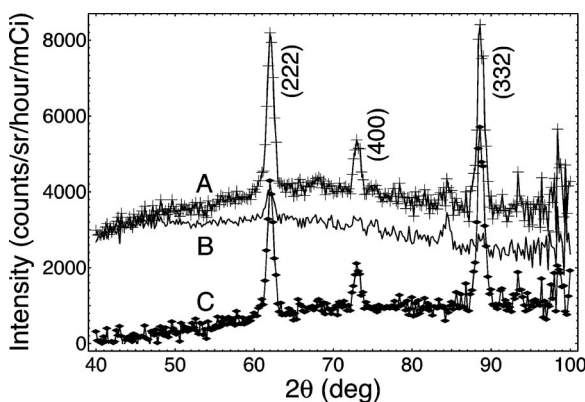


FIG. 1. On resonance (A), off resonance (B), and difference (C) traces for Mössbauer diffraction patterns of ^{57}Fe for transition $l=6$.

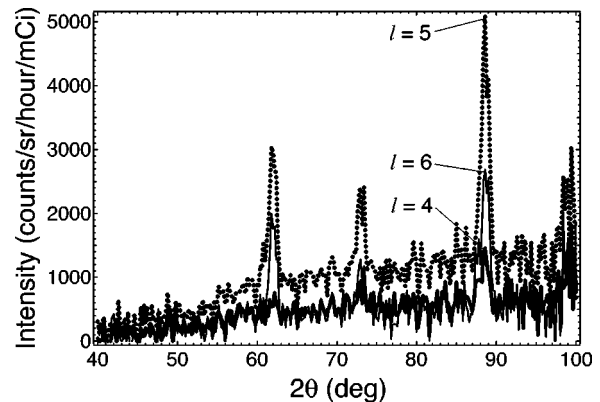


FIG. 3. In-field Mössbauer diffraction patterns of ^{57}Fe for transition lines $l=4$ (thick solid line), 5 (dotted line), and 6 (thin solid line).

TABLE I. Measured intensities when tuned to the peak of each of the six hyperfine transitions for diffraction (332). Units are counts(h mCi)⁻¹.

		$l=1$	$l=2$	$l=3$	$l=4$	$l=5$	$l=6$
Zero field	Diffuse	40.0	48.8	38.0	39.1	51.4	42.2
	Diffraction	12.9	7.01	3.32	2.94	7.39	11.5
In field	Diffuse	22.1	46.6	25.1	26.0	52.7	23.3
	Diffraction	7.98	10.0	1.54	2.02	10.2	6.64

incoherent Rayleigh scattering, Compton scattering, photoelectric absorption followed by x-ray emission, and contamination radiation including γ rays reaching the detector along paths other than scattering from the sample. The sharp peaks are from coherent diffraction of Rayleigh-scattered 6.4 keV and 14.41 keV photons. The on-resonance intensity (trace A) in Fig. 1 contains, in addition to photons scattered by the “nonresonant” mechanisms contributing to trace B, photons scattered by incoherent Mössbauer scattering (contributing to the smoothly varying component) and by Mössbauer diffraction (contributing to the sharp peaks). Three Mössbauer diffractions are visible: (222) at $2\theta=63^\circ$, (400) at $2\theta=74^\circ$, and (332) at $2\theta=89^\circ$. The other powder diffractions expected in the measured range of angles are weak or invisible, owing to crystallographic texture in the cold-rolled sample. (Texture was also evident from the discontinuous segments of diffraction cones recorded in the detector images.) If we assume that the Mössbauer attenuation in the sample has little effect on the number of photons scattered by non-Mössbauer mechanisms, the difference between the on-resonance and off-resonance curves provides an estimate of the intensity from Mössbauer-scattered photons. This method of subtracting the intensities in the two curves is not appropriate for removing the effects of Rayleigh diffraction on the Mössbauer diffraction peaks, however, since these two components are coherent and add in amplitude. This interference has a significant effect on the diffracted intensities and is handled more carefully below. Figure 2 shows the diffraction patterns obtained on resonance for three of the six lines. Figure 3 shows the $l=4$, 5, and 6 diffraction patterns obtained when an external magnetic field is applied so that the nuclear dipoles in the sample are aligned vertically. Over the full range of 2θ , the diffraction pattern for $l=5$ has more intensity than the patterns for $l=6$ and 4.

Although it is not strictly possible to separate coherent intensities originating with different scattering mechanisms, it is possible to separate the total coherent intensity from the measured data. Regions of 2θ away from the diffraction peaks were fit with a second-order polynomial that was subtracted from the data. (This fit function served as an approximation for the incoherent Mössbauer intensity and background.) The remaining intensities in the (222) or (332) diffraction were integrated, and much of the following discussion uses these intensities and their ratios.

Table I presents approximate incoherent and (332)-diffracted intensities on resonance for the six Mössbauer transitions, both in an external magnetic field and with no external field. As expected, the intensities are pairwise simi-

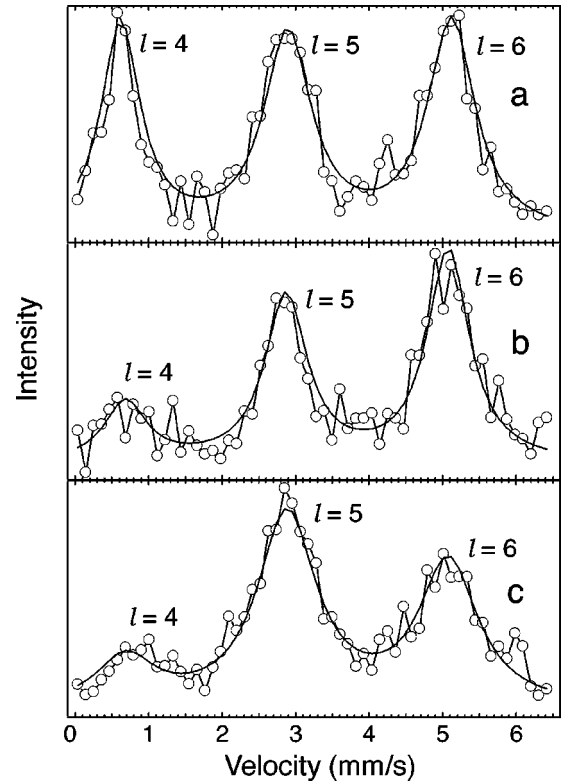


FIG. 4. Experimental energy spectra of Mössbauer diffraction intensities of ⁵⁷Fe for (a) zero-field diffuse scattering, (b) zero-field diffraction, and (c) in-field diffraction. Solid line is a Lorentzian fit to the data.

lar (e.g., the intensities for $l=1$ are similar to those for $l=6$), but this similarity is not perfect (e.g., the diffracted intensity for $l=1$ is larger than that for $l=6$). This lack of symmetry in the applied field is the direct result of the interference between the Mössbauer diffraction and the Rayleigh diffraction, and will be discussed in more detail below.

Diffraction patterns such as those in Figs. 1–3 were obtained at all velocities across the full Mössbauer spectrum of ⁵⁷Fe. The intensity as a function of Doppler drive velocity for incoherently scattered photons is shown in Fig. 4(a). Figure 4(b) shows the coherent intensity in the (332) diffraction without the external magnetic field, and Fig. 4(c) shows the (332) intensity with the magnetic field. In each case the intensity shows three peaks, corresponding to the $l=4$, 5, and 6 transitions of the ⁵⁷Fe sextet. Also shown in these figures is a sum of three Lorentzian lines, for which the line center energies and linewidths have been adjusted for the best fit to the experimental data. Without the external magnetic field, the intensity in the (332) or (222) diffractions is larger for the nuclear transitions $l=4$, $l=5$, and $l=6$, in sequence. With the external field, the diffracted intensity for $l=5$ is enhanced compared to those for $l=4$ and $l=6$.

IV. THEORY

A. Scattered intensities

We adapt the notation of Bara, developed for conventional backscatter Mössbauer spectra,^{16,17} and extend it to include

coherent interference. The extension must include the interaction between the polarization of the incident photon and the direction of the nuclear magnetic field, which has been described by van Bürck *et al.*¹⁸ Although Bara enumerates several interactions of photons with the sample, the only term applicable to diffraction is the backscattered intensity from recoilless scattering of recoilless source photons, I_{rr} .

With small differences in notation and including a polarization factor for the scattering angle 2θ , $W_\gamma(2\theta)$ of Balko and Hoy¹⁹ (discussed further in Sec. IV C),

$$I_{rr}(\beta_i, \beta_f, E) = \frac{f_1 W_\gamma(2\theta) \text{csc } \beta_i d\Omega_i d\Omega_f}{1 + \alpha} \times \int_{-\infty}^{\infty} dE_i \int_0^t dx R_{rr}(\beta_i, \beta_f, E, E_i, x), \quad (1)$$

where

$$R_{rr}(\beta_i, \beta_f, E, E_i, x) = U(E_i) \mu_r(E, E_i) \exp\{-x[\text{csc } \beta_i + \text{csc } \beta_f][\mu + \mu_r(E, E_i)]\}. \quad (2)$$

The subscripts i and f denote the incident and scattered photons, respectively. The angles of incidence and scattering with respect to the plane of the sample are β_i and β_f , and Ω_i and Ω_f are solid angles. The nuclear resonance energy of the ^{57}Fe nucleus is E . The energy spectrum of the source is $U(E_i)$, where E_i is the energy of the incident photon. The electronic absorption coefficient is μ , and $\mu_r(E, E_i)$ is the nuclear resonance absorption coefficient. The thickness of the sample is t , α is the internal conversion coefficient, and f_1 is the recoil-free fraction of the sample.

We generalize Eq. (1) for each nuclear transition l and hyperfine energy E as

$$I_{rrl}(\vec{k}_i, \vec{k}_f, E, E_i, x) = \xi_D \int_0^\infty dE_i \int_0^t dx R_{rrl}(\vec{k}_i, \vec{k}_f, E, E_i, x), \quad (3)$$

where

$$R_{rrl}(\vec{k}_i, \vec{k}_f, E, E_i, x) = \sum_{\nu_i, \nu_f} U(E_i) \exp\{-x[\mu + \mu_l(\vec{k}_i^{(\nu_i)}, E, E_i, \vec{u}_z)] \text{csc } \beta_i\} \times \frac{d\sigma_l}{d\Omega}(\vec{k}_i^{(\nu_i)}, \vec{k}_f^{(\nu_f)}, E, E_i, \vec{u}_z) \times \exp\{-x[\mu + \mu_l(\vec{k}_f^{(\nu_f)}, E, E_i, \vec{u}_z)] \text{csc } \beta_f\}. \quad (4)$$

Equation (4) includes factors for the spectrum of 14.4 keV photons, $U(E_i)$, for the attenuation by recoilless and nonrecoilless scattering as the photons penetrate into the sample to depth x , $\exp\{-x[\mu + \mu_l] \text{csc } \beta_i\}$, the cross section for nuclear resonant scattering, $d\sigma_l/d\Omega(\vec{k}_i^{(\nu_i)}, \vec{k}_f^{(\nu_f)}, E, E_i, \vec{u}_z)$, and a second exponential factor for attenuation as the scattered photons traverse the sample on the way out. Note that $d\sigma_l/d\Omega$, the cross section for resonant scattering by the l th

nuclear transition, depends on the incident and outgoing wave vectors $\vec{k}_i^{(\nu_i)}$ and $\vec{k}_f^{(\nu_f)}$, whereas the nuclear absorption cross section μ_l depends on only one of them. Here ν specifies the polarization state of the photon. Two orthogonal linear polarization states were used: $\nu=1$ denotes a photon electric field perpendicular to the scattering plane, and the electric field for $\nu=2$ is perpendicular to that of $\nu=1$. The unit vectors in the direction of the electric field and magnetic field of a photon are $\vec{e}^{(\nu)}$ and $\vec{h}^{(\nu)}$. The unit vector \vec{u}_z is along the direction of the nuclear hyperfine magnetic field. A sample-dependent constant ξ_D accounts for all factors common to diffraction from the six transitions in the ^{57}Fe sample, such as the variation in crystallite sizes and orientations, and includes the source recoil-free fraction, the internal conversion coefficient α , and the efficiency of the detector for 14.4 keV photons. Equations (3) and (4) neglect the coherency between l th and l' th transitions. This is acceptable for our ^{57}Fe sample because the splitting of hyperfine levels is much larger than the natural width.²⁰

B. Aligned hyperfine magnetic fields

The differential scattering cross section $d\sigma_l/d\Omega$ is obtained most easily when an applied magnetic field aligns the z axes of the hyperfine magnetic fields at all nuclei. The differential cross section originates with the coherent amplitudes from both nuclear resonant scattering and Rayleigh scattering,

$$\frac{d\sigma_l}{d\Omega} = |F_{\text{nuc}} + F_{\text{ele}}|^2, \quad (5)$$

where

$$F_{\text{nuc}} = \frac{\eta}{2} \frac{3}{2k(1+\alpha)} \sqrt{\frac{8\pi}{3}} [\vec{e}_i^{(\nu_i)} \cdot \vec{Y}_{1M}^{(m)}(\vec{n}_i)] \sqrt{\frac{8\pi}{3}} [\vec{e}_f^{(\nu_f)} \cdot \vec{Y}_{1M}^{(m)}(\vec{n}_f)]^* \times f_1 \frac{z_l(E_i) - i}{z_l(E_i) - i} C_l^2 \quad (6)$$

and

$$F_{\text{ele}} = -r_e F_e \vec{e}_i^{(\nu_i)} \cdot \vec{e}_f^{(\nu_f)}. \quad (7)$$

The enrichment of ^{57}Fe in the sample is η . The wave vector of the photon is k . The vector spherical harmonic for a magnetic [superscript “(m)”] dipole photon is $\vec{Y}_{1M}^{(m)}(\vec{n})$, where M is the angular momentum of the photon in the direction of the hyperfine magnetic field, and \vec{n} is the unit vector in the direction of photon propagation. The normalized energy shift is $z_l(E_i) = (2/\Gamma)(E_l - E_i)$, where E_l is the resonant energy for l th nuclear transition and Γ is the natural linewidth of the resonance. The Clebsch-Gordan coefficients are C_l . The classical electron radius is r_e , and F_e is the form factor for the electron clouds in a unit cell. The scattering amplitude is

a function of the incident and scattered polarizations \vec{h}_i and \vec{h}_f and of the nuclear hyperfine field direction \vec{u}_z through the polarization factors $p_l(\vec{h}, \vec{u})$,¹⁸

$$p_l(\vec{h}, \vec{u}) = -i \sqrt{\frac{8\pi}{3}} \vec{e} \cdot \vec{Y}_{1M}^{(m)}(\vec{n}) \quad (8)$$

$$= \vec{h} \cdot \vec{u}_l, \quad (9)$$

where \vec{u}_l is a spherical unit vector with a z component \vec{u}_z . The absorption cross section for the processes by which 14.4 keV photons are resonantly absorbed in the sample is obtained with the optical theorem

$$\mu_l(\nu, E, \vec{u}_z) = \frac{4\pi}{k} \text{Im} F_{\text{nuc}}(\vec{k}_f = \vec{k}_i). \quad (10)$$

C. Orientation distributions of hyperfine magnetic fields

To obtain the scattering intensity when no external field is applied to the sample, a model for the orientational distribution of the hyperfine magnetic field is needed. The differential scattering cross section can then be obtained by averaging over all nuclei. It consists of three contributions: nuclear scattering, Rayleigh scattering, and their interference:

$$\frac{d\bar{\sigma}_l}{d\Omega} = \frac{d\bar{\sigma}_{\text{nuc}}}{d\Omega} + \frac{d\bar{\sigma}_{\text{ele}}}{d\Omega} + \frac{d\bar{\sigma}_{\text{int}}}{d\Omega}, \quad (11)$$

where

$$\frac{d\bar{\sigma}_{\text{nuc}}}{d\Omega} = |F_{\text{nuc}}^0|^2 \bar{P}_{\text{nuc}}^2, \quad (12)$$

$$\frac{d\bar{\sigma}_{\text{ele}}}{d\Omega} = |F_{\text{ele}}^0|^2 |P_{\text{ele}}|^2, \quad (13)$$

$$\frac{d\bar{\sigma}_{\text{int}}}{d\Omega} = 2 \text{Re}[(F_{\text{ele}}^0)^* F_{\text{nuc}}^0 P_{\text{ele}}^* \bar{P}_{\text{nuc}}], \quad (14)$$

and

$$F_{\text{nuc}}^0 = \frac{\eta}{2} \frac{3}{2k(1+\alpha)} f_1 \frac{1}{z_l(\omega) - i} C_l^2, \quad (15)$$

$$F_{\text{ele}}^0 = -r_e F_e, \quad (16)$$

$$P_{\text{ele}} = \vec{e}_i \cdot \vec{e}_f. \quad (17)$$

The absorption cross section is given by

$$\bar{\mu}_l = \mu_l^0 \bar{P}_{\text{nuc}}(2\theta=0), \quad (18)$$

where $\mu_l^0 = (4\pi/k) \text{Im} F_{\text{nuc}}^0$.

Calculating the scattered intensity for unpolarized incident radiation requires evaluating the averages \bar{P}_{nuc}^2 and \bar{P}_{nuc} , which are the polarization factors of Eq. (8) averaged over the orientations of nuclear magnetic dipoles. Calculating $d\bar{\sigma}_{\text{int}}/d\Omega$ of Eq. (14), for example, requires averaging

the $p_l(\vec{h}, \vec{u})$ over the orientation distribution of the hyperfine magnetic fields (HMF's). This is performed formally with the rotation matrices and operators \mathbf{R} and $\mathbf{P}_{\mathbf{R}}$ as

$$\bar{P}_{\text{nuc}} = \int d\vec{R} \rho(\mathbf{R}\vec{u}_z^0) \mathbf{P}_{\mathbf{R}} [p_l(\vec{h}_i, \vec{u}) [p_l(\vec{h}_f, \vec{u})]^*], \quad (19)$$

and similarly for \bar{P}_{nuc}^2 . It is convenient to expand the distribution function, $\rho(\mathbf{R}\vec{u}_z^0)$, in spherical harmonics, $Y_{\lambda\mu}$, with expansion coefficients $a^{\lambda\mu}$. The values of \bar{P}_{nuc}^2 and \bar{P}_{nuc} are

$$\bar{P}_{\text{nuc}}^2 = \sum_{\lambda\mu} a^{\lambda\mu} \bar{P}_{\lambda\mu;\text{nuc}}^2, \quad (20)$$

$$\bar{P}_{\text{nuc}} = \sum_{\lambda\mu} a^{\lambda\mu} \bar{P}_{\lambda\mu;\text{nuc}}. \quad (21)$$

For each spherical harmonic, $\bar{P}_{\lambda\mu;\text{nuc}}^2$ and $\bar{P}_{\lambda\mu;\text{nuc}}$ can be obtained analytically using results for the rotation matrices $\mathcal{D}_{m'm}^j(\alpha\beta\gamma)$,²¹

$$\begin{aligned} \bar{P}_{\lambda\mu;\text{nuc}}^2 &= \frac{1}{4} \sqrt{\frac{2\lambda+1}{4\pi}} \sum_{m_i, m_i', m_f, m_f'} J_{\lambda\mu}(m_i, m_f, m_i', m_f') [\delta_{1m_i} \\ &+ (-1)^{\nu_i-1} \delta_{-1, m_i'}] [\delta_{1m_i'} + (-1)^{\nu_i-1} \delta_{-1, m_i'}] \\ &\times \left[\mathcal{D}_{1m_f}^1\left(\frac{\pi}{2}, 2\theta, -\frac{\pi}{2}\right) + (-1)^{\nu_f-1} \right. \\ &\times \mathcal{D}_{-1, m_f}^1\left(\frac{\pi}{2}, 2\theta, -\frac{\pi}{2}\right) \left. \right] \left[\mathcal{D}_{1m_f'}^1\left(\frac{\pi}{2}, 2\theta, -\frac{\pi}{2}\right) \right. \\ &\left. + (-1)^{\nu_f-1} \mathcal{D}_{-1, m_f'}^1\left(\frac{\pi}{2}, 2\theta, -\frac{\pi}{2}\right) \right]^*, \end{aligned} \quad (22)$$

$$\begin{aligned} \bar{P}_{\lambda\mu;\text{nuc}} &= \frac{1}{6} \sqrt{\frac{2\lambda+1}{4\pi}} \sum_{m_i, m_f} C_{m_f, \mu, m_i}^{1, \lambda, 1} C_{M, 0, M}^{1, \lambda, 1} [\delta_{1m_i} \\ &+ (-1)^{\nu_i-1} \delta_{-1, m_i}] \left[\mathcal{D}_{1m_f}^1\left(\frac{\pi}{2}, 2\theta, -\frac{\pi}{2}\right) \right. \\ &\left. + (-1)^{\nu_f-1} \mathcal{D}_{-1, m_f}^1\left(\frac{\pi}{2}, 2\theta, -\frac{\pi}{2}\right) \right]^*, \end{aligned} \quad (23)$$

where

$$\begin{aligned} J_{\lambda\mu} &= \sum_{j=0,1,2} \frac{1}{2j+1} \\ &\times \sum_{j'=0,1,2} C_{m_i, m_f, m_i+m_f}^{1,1,j} C_{m_i', m_f', m_i'+m_f'}^{1,1,j'} C_{M, M, 2M}^{1,1,j} \\ &\times C_{M, M, 2M}^{1,1,j'} C_{m_i'+m_f', \mu, m_i+m_f}^{j', \lambda, j} C_{2M, 0, 2M}^{j', \lambda, j}, \end{aligned} \quad (24)$$

and 2θ is the diffraction angle. The averaged polarization factors $\bar{P}_{\lambda\mu;\text{nuc}}^2$ and $\bar{P}_{\lambda\mu;\text{nuc}}$ vanish when λ is large ($\lambda > 4$ for \bar{P}^2 , $\lambda > 2$ for \bar{P}). The polarization factors are therefore in-

TABLE II. Polarization factors for Mössbauer scattering averaged over hyperfine magnetic field distributions. The two distributions— isotropic and anisotropic with a planar bias—are described in the text.

Transitions	Polarization index		Averaged polarization factor \bar{P}_{nuc}^2	
	Incident	Outgoing	Isotropic	Planar bias
$M_i = M_f = \pm 1$	1	1	$\frac{1}{10} + \frac{1}{30} \cos^2(2\theta)$	$\frac{1}{70} \{9 + \cos(2\beta_i) + \cos(2-2\theta) + \cos[2(\beta_i - 2\theta)]\}$
	1	2	$\frac{1}{10}$	$\frac{1}{140} [13 + 3 \cos(2\beta_i)]$
	2	1	$\frac{1}{10}$	$\frac{1}{140} \{13 + 3 \cos[2(\beta_i - 2\theta)]\}$
	2	2	$\frac{2}{15}$	$\frac{4}{35}$
$M_i = M_f = 0$	1	1	$\frac{1}{15} + \frac{2}{15} \cos^2(2\theta)$	$\frac{1}{70} \{8 - 3 \cos(2\beta_i) + 4 \cos(2-2\theta) - 3 \cos[2(\beta_i - 2\theta)]\}$
	1	2	$\frac{1}{15}$	$\frac{1}{70} [5 - \cos(2\beta_i)]$
	2	1	$\frac{1}{15}$	$\frac{1}{70} \{5 - \cos[2(\beta_i - 2\theta)]\}$
	2	2	$\frac{1}{5}$	$\frac{9}{35}$

Transitions	Polarization index		Averaged polarization factor \bar{P}_{nuc}	
	Incident	Outgoing	Isotropic	Planar bias
$M_i = M_f = \pm 1$	1	1	$\frac{1}{3} \cos(2\theta)$	$\frac{1}{20} [7 \cos(2\theta) + \cos(2\beta_i - 2\theta)]$
	1	2	0	0
	2	1	0	0
	2	2	$\frac{1}{3}$	$\frac{3}{10}$
$M_i = M_f = 0$	1	1	$\frac{1}{3} \cos(2\theta)$	$\frac{1}{10} [3 \cos(2\theta) - \cos(2\beta_i - 2\theta)]$
	1	2	0	0
	2	1	0	0
	2	2	$\frac{1}{3}$	$\frac{2}{5}$

sensitive to sharp angular variations in the HMF distribution (which require higher-order spherical harmonics).

We obtained polarization factors for two specific distributions of hyperfine magnetic field orientations. The first is an isotropic distribution of hyperfine magnetic fields in the sample. With the isotropic model we confirmed the prior results for \bar{P}_{nuc}^2 of Balko and Hoy.²² The other “anisotropic” model biased the hyperfine magnetic fields in the plane of the sample surface:

$$\rho_{\text{planar}}(\vec{u}_z) = \frac{3}{2} [1 - (\vec{u}_z \cdot \hat{n}_S)^2], \quad (25)$$

where \hat{n}_S is the normal of the sample surface. Since the angle between \hat{n}_S and \vec{k}_i is $\pi/2 - \beta_i$, we obtain the following expansion coefficients:

$$a^{00} = 2\sqrt{\pi}, \quad (26)$$

$$a^{20} = \sqrt{\frac{\pi}{20}} (-1 + 3 \cos 2\beta_i), \quad (27)$$

$$a^{2,\pm 1} = i \sqrt{\frac{3\pi}{10}} \sin 2\beta_i, \quad (28)$$

$$a^{2,\pm 2} = \sqrt{\frac{3\pi}{10}} \cos^2 \beta_i. \quad (29)$$

Table II presents the results for averaged polarization factors \bar{P}_{nuc}^2 and \bar{P}_{nuc} for both the isotropic and the anisotropic HMF distribution models, obtained from Eqs. (20) and (21) with appropriate $a^{\lambda\mu}$. These \bar{P}_{nuc}^2 and \bar{P}_{nuc} play a role somewhat analogous to the Lorentz polarization factor of x-ray powder diffractometry, although their angular dependence is dominated by the effects of the orientations of the hyperfine magnetic fields at the nuclei as shown in Table II.

D. Calculations

To obtain the intensity I_{rrl} measured at the detector when the Doppler drive is tuned to an isolated l th nuclear transition, the differential scattered flux $R_{rrl}(\vec{k}_i, \vec{k}_f, E, E_i, x)$ was summed over the polarization states ν_i and ν_f , and integrated analytically over the thickness t and numerically over the source spectrum E_i . Results for I_{rrl} were obtained for each nuclear transition l, E . The following values were used for the constants in the calculation. The internal conversion coefficient was $\alpha = 8.21$, the recoil-free fraction was $f_1 = 0.8$, the absorption coefficient μ from nonresonant processes was 539.0 cm^{-1} , the thickness of the sample $t = 2.55 \mu\text{m}$, the scattering angle $\beta_i + \beta_f$ was 89° for the (332) diffraction and 63° for the (222) diffraction, and the angle β_i was 39° . The only adjustable parameter was ξ_D . Results from this calculation are shown with the corresponding experimental results in Table III. For the (222) and (332) diffractions, we compare the ratios of their intensities for different values of $l, D_{l_i:l_j} \equiv I_{rrl_i}/I_{rrl_j}$.

TABLE III. Comparison of experimental and calculated ratios $D_{l_i:l_j}$ of diffracted intensities for the hyperfine transitions l_i and l_j . Results are presented for the (332) and (222) diffractions, both with and without an external magnetic field. There are two calculated ratios when no external field is applied to the sample; the first number is calculated for an isotropic hyperfine magnetic field distribution, and the second is for the planar-biased distribution described in the text.

	$D_{2:1}$		$D_{3:1}$		$D_{4:6}$		$D_{5:6}$	
(332)	Observed	Calculated	Observed	Calculated	Observed	Calculated	Observed	Calculated
Zero field	0.54	0.60/0.67	0.26	0.31/0.31	0.26	0.31/0.31	0.64	0.60/0.66
In field	1.26	1.28	0.19	0.23	0.30	0.45	1.46	1.53
(222)	Observed	Calculated	Observed	Calculated	Observed	Calculated	Observed	Calculated
Zero field	0.61	0.65/0.60	0.36	0.33/0.33	0.38	0.33/0.33	0.70	0.63/0.58
In field	1.40	1.43	0.34	0.33	0.47	0.43	1.37	1.39

V. DISCUSSION

In addition to resonant emission from resonant scattering, I_{rr} (generalized in Sec. IV A to include x-ray Rayleigh scattering and coherent effects), we also calculated the contributions to the broad incoherent intensity shown in Figs. 1(c), 2, and 3. Processes contributing to this incoherent background include resonant and nonresonant scattering of recoilless 14.4 keV γ rays (denoted I_{rr}, I_{rn}) and nonresonant scattering of nonrecoilless 14.4 keV γ rays (denoted I_{nn}). The detector had an aluminum filter to suppress its sensitivity to 6 keV x rays, but a minor contribution is also expected from internal conversion processes (a contribution to I_{rn}), scattering of x rays from the source (a contribution to I_{nn}), and sample fluorescence. The processes contributing to I_{nn} are removed when the off-resonance diffractograms are subtracted from the on-resonance diffractograms, but the I_{rn} requires a more thorough analysis. This has proved challenging, and our analysis is still underway. Some experimental results on incoherent scattering are presented in Table I.

Table I presents diffraction intensities on resonance, normalized by incident flux, and we can use them for comparing the intensities of diffraction peaks with and without the applied magnetic field. We find that the intensities in the magnetic field are systematically larger than that of the calculation by a factor of 1.7, and this was confirmed by remounting the sample several times. This enhancement was also observed in the off-resonance diffractograms, however, so we must assume that it originates with variations in the factor ξ_D of Eq. (3). Using this factor of 1.7, the predicted diffraction intensities agreed with measurements to within a few percent. The large effect of the applied magnetic field on the intensity of the $l=2,5$ transitions is similar to that in conventional Mössbauer spectroscopy.

More accurate measurements of the effect of the magnetic field on powder diffraction intensities from polycrystals can be made by comparing the relative intensities of a diffraction peak with the Doppler drive tuned to resonance conditions. Calculation and experiment both show that the diffracted intensity from the $l=2,5$ transitions are larger relative to the $l=1,6$ and $l=3,4$ transitions when a vertical magnetic field is applied to the sample. This can also be seen by comparing Figs. 4(b) and 4(c). For the $l=2,5$ transition for which \vec{u}_l

$=\vec{u}_z$, Eq. (9) shows that $p_l(\vec{h}, \vec{u}_z)=0$ when \vec{h} is in the plane perpendicular to \hat{z} . Since $\vec{h}\perp\vec{k}$, there is zero amplitude for the $l=2,5$ transition along the z direction. The diffracted intensity in the plane of scattering (which is perpendicular to the direction \vec{u}_z) is instead enhanced for $l=2,5$, compared to those for $l=1,6$ and $l=3,4$.

A near-isotropic photon emission was calculated with both the isotropic and planar models for the distributions of hyperfine magnetic fields. We can therefore estimate the magnitude of the effect of the applied magnetic field as follows. When the sample is 2 or 3 times thicker than the extinction length, the scattering intensity can be approximated as^{4,9}

$$I_{rrl} \propto \frac{d\sigma/d\Omega}{\mu}. \quad (30)$$

When the source is tuned to a nuclear resonance, we can ignore the Rayleigh scattering and interference in our approximation, so we have $\sigma \propto \bar{P}_{\text{nuc}}^2$ and $\mu \propto \bar{P}_{\text{nuc}}(2\theta=0)$. The scattering intensity is therefore proportional to

$$I_{rrl} \propto \frac{\bar{P}_{\text{nuc}}^2}{\bar{P}_{\text{nuc}}(2\theta=0)}. \quad (31)$$

For both the isotropic and anisotropic distributions of hyperfine magnetic fields, at the diffraction angles of $2\theta=63^\circ$ and $2\theta=89^\circ$ we found that the value of $\bar{P}_{\text{nuc}}^2[\bar{P}_{\text{nuc}}(2\theta=0)]^{-1}$, averaged over the polarization states, is approximately $\frac{2}{3}$ for both $M=\pm 1$ and $M=0$. On the other hand, if all nuclear magnetic moments are in the same direction, then the value of $\bar{P}_{\text{nuc}}^2/\bar{P}_{\text{nuc}}(2\theta=0)$ averaged over the polarization states is $\frac{1}{4}$ if $M=\pm 1$ and $\frac{1}{2}$ if $M=0$. Transitions 2 and 5 are therefore favored when an external magnetic field is applied to the sample in a direction perpendicular to the scattering plane. This is approximately consistent with the results in Table I. The predicted intensities are smaller in the presence of the magnetic field because incident photons of one polarization are not absorbed.

The difference in intensity of diffraction peaks for the $l=1$ and the $l=6$ transitions (see Fig. 5) in an applied mag-

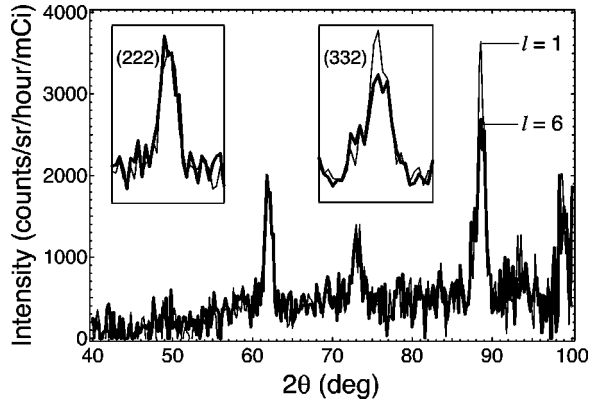


FIG. 5. In-field diffraction patterns for transition lines $l=1$ (thin solid line) and $l=6$ (thick solid line). The symmetry that exists in the transmission spectrum is broken.

netic field has no analog in conventional Mössbauer spectroscopy. The origin of this asymmetry of the energy spectrum is the effect of interference between nuclear and Rayleigh scattering, in which the phase^{23,24} of the polarization factor plays an important role. Notice that the phase in Eq. (6) for $1/[z_l(E_i) - i]$ is $\pi/2$ when $E_i = E$, and the phase for $p_l(\vec{h}_i, \vec{u})[p_l(\vec{h}_f, \vec{u})]^*$ is $\pm 2\theta$ when $l=1,6$. The phase difference between F_{nuc} and F_{ele} is therefore $(3\pi/2 \pm 2\theta)$ for $l=1,6$. For the (332) diffraction, the scattering intensities are then approximately $(|F_{\text{nuc}}| \pm |F_{\text{ele}}|)^2$ for $l=1,6$. From tabulated x-ray form factors,¹⁴ $|F_{\text{ele}}|$ is estimated to be about 4% of $|F_{\text{nuc}}|$. Thus, $I_{rr1} > I_{rr6}$ and the asymmetry is about 16%. This estimate is in approximate agreement with our measurements and the results in Table III from the more complete calculation.

Equation (6) accounts for “spin-flip incoherence.” In Eq. (6) the incident and scattered photons have the same quantum number for their angular momentum in the direction of hyperfine magnetic field. If the scattering involved a change in photon angular momentum, the angular momentum of the nuclear ground state would be altered, “tagging” the excited nucleus and preventing coherence with other nuclei. If we intentionally evaluate Eq. (6) with a spin-flip process, i.e., $\vec{Y}_{1M'}^{(m)}(\vec{n}_f)$ differing from $\vec{Y}_{1M}^{(m)}(\vec{n}_i)$, we find that the scattering amplitude has a phase factor that depends on the choice of the coordinate system—the phase factor is not well defined. Scattering from a nucleus without a well-defined phase cannot be coherent with scattering from other nuclei, so spin-flip processes are incoherent.²⁵ The spin-flip incoherence reduces the diffraction intensity, and the reduction is accounted for by the Clebsch-Gordan coefficients. For example, when E_i is tuned to line 3, the nuclear scattering amplitude F_{nuc} is reduced by a factor of $C_3^2 = \frac{1}{3}$. Hence, the scattering cross section is reduced by a factor of $\frac{1}{9}$. Considering the reduction also applies to absorption processes, the diffraction intensity is reduced by a factor of $\frac{1}{9} / \frac{1}{3} = \frac{1}{3}$.

The validity of our analysis of the effect of an externally applied field requires that dynamical diffraction effects be small, since in the presence of dynamical diffraction, the intensity in a given diffraction peak cannot be easily interpreted in terms of the scattering factors in the sample. Fig-

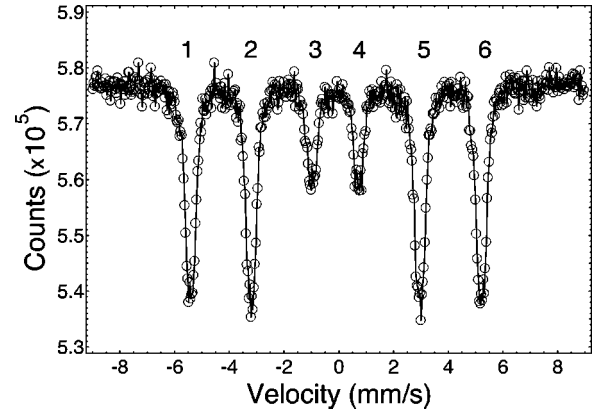


FIG. 6. Mössbauer spectrum in transmission from natural Fe.

ures 4(a) and 4(b) show diffracted and incoherent intensities as a function of Doppler drive velocity. The peak diffracted counts plotted in Fig. 4(a) were estimated by summing the (332)-diffracted intensity over a 2° range and dividing by an estimated peak width of 0.8° . Both of these curves were fit with a sum of Lorentzian functions to estimate the measured linewidths. The linewidths for the diffracted intensity ($0.40 \pm 0.04 \text{ mm s}^{-1}$) do not differ significantly from those for incoherent intensity ($0.44 \pm 0.04 \text{ mm s}^{-1}$). This upper limit (of perhaps 10%) on broadening is consistent with the dynamical broadening which one expects in a sample with a mean crystal size of one extinction length or less. We conclude that in our sample dynamical effects could be small, but this cannot be proved from the line shape analysis because one extinction length might be significant. More careful measurements would be required to prove that dynamical effects are in fact insignificant.

The linewidths obtained by the fitting analysis are broader than the intrinsic linewidth by a factor of about 4. This is probably due to absorption saturation²⁶ in the sample. For reference, Fig. 6 shows a conventional Mössbauer transmission spectrum of natural iron taken using the Doppler drive setup described above, with a photomultiplier tube as detector. The linewidth obtained by fitting the dips with Lorentzians is 0.2 mm s^{-1} , significantly smaller than the linewidths in Figs. 4(a) and 4(b).

VI. CONCLUSIONS

Instrumentation was developed to measure ^{57}Fe Mössbauer diffractions with sufficient precision so that differences in the intensities of diffraction peaks could be determined reliably for polycrystalline samples. Measurements were performed with and without the presence of an applied magnetic field at the sample, and large effects were observed in the relative intensities of the peaks 2 and 5 of the ferromagnetic sextet.

Calculations of the ^{57}Fe diffraction intensities in the single-scattering (kinematical) approximation were performed as a function of Bragg angle, accounting for electronic and nuclear absorption and scattering. The analysis included the effects of nuclear polarization, and a complete analysis was performed for three orientation distributions of

hyperfine magnetic fields: (1) uniaxial, (2) isotropic, and (3) anisotropic with cylindrical symmetry. There was good agreement between the calculated and measured intensities of the diffraction peaks when different nuclear resonance conditions were used for the same sample configuration. Reasonable agreement was found between the calculated and measured effects of the applied magnetic field on the diffraction intensities.

It was found that the Mössbauer transitions of opposite angular momentum, such as peaks 1 and 6 of the magnetic sextet, are of unequal intensities in the presence of an applied magnetic field owing to interference with Rayleigh scattering.

We confirmed the presence of spin flip incoherence for excitations 2 and 5 of the magnetic sextet. These transitions

can undergo a magnetic dipole decay to a different ground state after excitation, forcing incoherence.

The intensities of the diffraction intensities were measured at different Doppler shifts, providing an energy spectrum of coherent intensity. The linewidths of these energy spectra were broadened considerably by thickness distortion, but there was no evidence of extra broadening at the angles of strong Bragg diffraction. It seems that dynamical effects were not significant in these polycrystalline materials.

ACKNOWLEDGMENT

This work was supported by the U.S. National Science Foundation under Contract No. DMR-9816617.

-
- ¹P. J. Black and P. B. Moon, *Nature (London)* **188**, 481 (1960).
²P. J. Black, G. Longworth, and D. A. O'Connor, *Proc. Phys. Soc. London* **83**, 925 (1964).
³Yu. Kagan, A. M. Afanas'ev, and I. P. Perstnev, *Zh. Éksp. Teor. Fiz* **54**, 1530 (1968) [*Sov. Phys. JETP* **27**, 819 (1968)].
⁴J. P. Hannon and G. T. Trammell, *Phys. Rev.* **186**, 306 (1969).
⁵Yu. Kagan, *Hyperfine Interact.* **123/124**, 83 (1999).
⁶J. P. Hannon and G. T. Trammell, *Hyperfine Interact.* **123/124**, 127 (1999).
⁷G. V. Smirnov and A. I. Chumakov, in *Resonant Anomalous X-ray Scattering*, edited by G. Materlik, C. J. Sparks, and K. Fischer (Elsevier, Amsterdam, 1994), p. 609, and references therein.
⁸U. van Bürck *et al.*, *Phys. Rev. Lett.* **59**, 355 (1987).
⁹D. A. O'Connor and P. J. Black, *Proc. Phys. Soc. London* **83**, 941 (1964).
¹⁰V. A. Belyakov, *Usp. Fiz. Nauk* **115**, 553 (1975) [*Sov. Phys. Usp.* **18**, 267 (1975)].
¹¹M. Tegze and G. Faigel, *Hyperfine Interact.* **92**, 1143 (1994); G. Faigel and M. Tegze, *ibid.* **92**, 1137 (1994).
¹²T. A. Stephens, W. Keune, and B. Fultz, *Hyperfine Interact.* **92**, 1095 (1994).
¹³T. A. Stephens and B. Fultz, *Phys. Rev. Lett.* **78**, 366 (1997); B. Fultz and T. A. Stephens, *Hyperfine Interact.* **113**, 199 (1998); T. A. Stephens, Ph.D. thesis, California Institute of Technology, 1996.
¹⁴B. Fultz and J. M. Howe, *Transmission Electron Microscopy and Diffractometry of Materials* (Springer-Verlag, Heidelberg, 2000), Chap. 1.
¹⁵U. Kriplani, M. W. Regehr, and B. Fultz, *Hyperfine Interact.* (to be published); U. Kriplani, Ph.D. thesis, California Institute of Technology, 2000.
¹⁶J. J. Bara, *Phys. Status Solidi A* **58**, 349 (1980).
¹⁷Z. Mei, B. Fultz, and J. W. Morris, Jr., *J. Appl. Phys.* **64**, 2550 (1988).
¹⁸U. van Bürck, G. V. Smirnov, R. L. Mössbauer, F. Parak, and N. A. Semioschkina, *J. Phys. C* **11**, 2305 (1978).
¹⁹B. Balko and G. Hoy, *Phys. Rev. B* **10**, 4523 (1974).
²⁰Y. Nakai, Y. Ooi, and K. Kunitomi, *J. Phys. Soc. Jpn.* **57**, 3172 (1988).
²¹M. E. Rose, *Elementary Theory of Angular Momentum* (Dover, New York, 1995).
²²B. Balko and G. Hoy, *Phys. Rev. B* **10**, 36 (1974).
²³D. E. Brown, J. Arthur, A. Q. R. Baron, G. S. Brown, and S. Shastri, *Phys. Rev. Lett.* **69**, 699 (1992).
²⁴D. P. Siddons, U. Bergmann, and J. B. Hastings, *Phys. Rev. Lett.* **70**, 359 (1993).
²⁵A. N. Artem'ev, V. V. Sklyarevskii, G. V. Smirnov, and E. P. Stepanov, *Sov. Phys. JETP* **36**, 736 (1973).
²⁶S. Margulies and J. R. Ehrman, *Nucl. Instrum. Methods* **12**, 131 (1961).